ARTICLE

Check for updates

Nuclear linear-chain structure arises in carbon-14

Jiaxing Han [1,2], Yanlin Ye [1✉], Jianling Lou [1], Xiaofei Yang [1], Qite Li[1], Zaihong Yang [1], Yanyun Yang[3], Jiansong Wang [3,4], Jinyan Xu[1], Yucheng Ge[1], Hui Hua[1], Zhihuan Li[1], Biao Yang[1], Yang Liu[1,2], Shiwei Bai[1], Kai Ma[1], Jiahao Chen [1], Gen Li[1], Ziyao Hu[1], Hanzhou Yu[1], Zhiwei Tan[1], Lisheng Yang[1], Shujing Wang[1], Longchun Tao[1], Wei Liu[1], Ying Jiang[1,2], Jingjing Li[1], Dongxi Wang[1], Siwei Huang[1], Ying Chen[1], Weiliang Pu[1], Kang Wei[1], Junbing Ma[3], Herun Yang[3], Peng Ma[3], Shiwei Xu[3], Zhen Bai[3], Shuya Jin[3], Fangfang Duan[3], Yushou Song[5], Liyuan Hu[5], Yao Li[5], Junwei Li[5], Suyalatu Zhang[6], Meirong Huang[6], Dexin Wang[6] & Ziming Li [7]

The shape and internal structure of an atomic nucleus can change significantly with increasing excitation energy, angular momentum, or isospin asymmetry. As an example of this structural evolution, linear-chain configurations in carbon or heavier isotopes have been predicted for decades. Recent studies have found non-stability of this structure in ^{12}C while evidenced its appearance in ^{16}C. It is then necessary to investigate the linear-chain molecular structures in ^{14}C to clarify the exact location on the nuclear chart where this structure begins to emerge, and thus to benchmark theoretical models. Here we show a cluster-decay experiment for ^{14}C with all final particles coincidentally detected, allowing a high Q-value resolution, and thus a clear decay-path selection. Unambiguous spin-parity analyses are conducted, strongly evidencing the emergence of the π-bond linear-chain molecular rotational band in ^{14}C. The present results encourage further studies on even longer chain configurations in heavier neutron-rich nuclei.

[1] School of Physics and State Key Laboratory of Nuclear Physics and Technology, Peking University, 100871 Beijing, China. [2] Institute of Materials, China Academy of Engineering Physics, 621907 Mianyang, China. [3] Institute of Modern Physics, Chinese Academy of Sciences, 730000 Lanzhou, China. [4] School of Science, Huzhou University, 313000 Huzhou, China. [5] Fundamental Science on Nuclear Safety and Simulation Technology Laboratory, Harbin Engineering University, 150001 Harbin, China. [6] Institute of Nuclear Physics, Inner Mongolia Minzu University, 028000 Tongliao, China. [7] School of Physics, Beihang University, 100191 Beijing, China. ✉email: yeyl@pku.edu.cn

The atomic nucleus is generally regarded as a compact quasi-sphere composed of nucleons (neutrons and protons) moving almost independently inside a self-consistent mean field[1,2]. However, the shape and internal structure configuration of a nucleus can be dramatically changed with increasing excitation energy, angular momentum or isospin asymmetry (i.e., neutron-to-proton ratio)[3]. Along this trend of structural evolution, one prominent scenario is the formation of the intriguing cluster or molecular configurations within the nucleus, as a result of the competition between the central global interaction and the local few-nucleon correlations[3–7]. One noticeable example for nuclear clustering is the 3-α condensation-type structure of the 0_2^+ state in ^{12}C (the well-known Hoyle state)[6], which plays a crucial role in the synthesis of heavier elements in stars and thereby the creation of the carbon-based life on earth. As a matter of fact, clustering phenomena appear at every level of the matter universe, from the largest galaxy systems[8] to the smallest hadronic systems[9].

Over the years, a number of physics concepts have been revealed for describing the cluster formation in nuclei, including the threshold effect[4], strong nucleon correlations in a low-density environment together with the possible appearance of the Bose–Einstein condensation (BEC) states[6,10–12], wave-pocket description of nuclear structures with configuration mixing[13–15], as well as the orthogonality of quantum states driven by the valence neutron occupancy[13–16]. The local nucleon correlations and the cluster interactions should also serve as testing grounds for ab initio-type nuclear forces rooted in Quantum Chromodynamics (QCD)[17].

Despite the tremendous theoretical progress for both stable and unstable nuclei, firm experimental evidences of cluster (or molecular) structures in light nuclei are still very limited, due basically to the difficulties in identifying the cluster states from the overwhelmingly large number of single-particle states. Originally, inclusive missing-mass measurements were performed, which allow to speculate on the possible molecular rotational bands by excluding the states already classified into the single-particle scheme[3]. Over the past two decades, the application of the coincident measurements of the decay fragments has allowed to selectively access the resonant states with strong cluster structure, to reconstruct their resonant energies, and to probe their spin-parities via the model-independent angular correlation analysis[18,19]. These latter two quantities, excitation energy versus spin, are necessary to identify the cluster (or molecular) rotational bands characterized by their typically large moment of inertia. For reactions involving unstable secondary beams in inverse kinematics, the position-sensitive detection at very forward angles, using such as our state-of-the-art zero-degree telescope[19–21], is essential to record the decay fragments with high efficiency. This kind of measurements has assured the discovery of a few molecular rotational bands having 2-α-core configurations in neutron-rich beryllium isotopes (Fig. 1a)[18,19].

More abundant cluster configurations can be expected for carbon isotopes featured by 3-α cores, which might be linearly aligned corresponding to the largest moment of inertia[3,13–16,22]. This linear-chain structure was initially proposed for the 0_2^+ state of ^{12}C (the Hoyle state)[23]. But recent studies have found the non-stability of the chain structure in ^{12}C[13,14] while evidenced its appearance in neutron-rich ^{16}C[20,21]. It is then crucial to search for the linear-chain molecular bands in ^{14}C in order to clarify the exact location on the nuclear chart where this exotic chain structure may begin to emerge (see the illustration in Fig. 1a) and thus to benchmark the theoretical models.

Compared to the previous works on the beryllium isotopes with the 2-α cores, experimental investigations of the 3-α-core carbon systems are obviously more challenging. Here, the decay fragments, such as ^{10,12}Be, may have bound excited states. Hence, the

conversion from the measured relative-energy spectrum to the physically meaningful excitation-energy spectrum necessarily depends on the specific states of the decaying fragments, corresponding to different reaction Q-values[20,21,24]. Indeed, a series of the breakup reaction (excitation followed by cluster-decay) experiments, dedicated to the simultaneous reconstruction of the relative energy and the reaction Q-value, have been undertaken to search for the linear-chain structures in ^{14}C[24–31]. These measurements generated consistent resonant energies but little information on the spin-parities due basically to the limited resolutions or statistics[29,32]. In recent years, a few resonant scattering experiments were also conducted for ^{14}C using the thick-target (^{4}He gas) technique[33–35]. However, they are generally not able to measure the reaction Q-values, and consequently, the reported resonant state at certain excitation energy (e.g. the one ~15 MeV[35]) might have been mixed with strongly populated states at higher energies (see further discussion below). Indeed, the spin-parity assignments from these experiments often contradict each other and those from the breakup experiments[29,33–35]. Therefore, the existence of the linear-chain structures in ^{14}C still remains uncertain.

In order to identify the possible linear-chain molecular band in ^{14}C, we have performed an inelastic-excitation and cluster-decay experiment. Through the coincident detection of all final particles with high efficiencies, we achieved a high Q-value resolution, enabling a clear selection of the decay paths. The resonances correspond to the first three members of the predicted π-bond linear-chain molecular rotational band in ^{14}C were observed and unambiguous spin-parity analyses were conducted. The present results provide strong evidence for the emergence of the chain structure starting from ^{14}C.

Results and discussion

Experimental set-up and detection methods. This experiment was carried out at the Radioactive Ion Beam Line at the Heavy Ion Research Facility in Lanzhou (HIRFL-RIBLL1)[36], and the targeted reaction channel is ^{1}H(^{14}C,^{14}C*$\rightarrow ^{10}$Be + α)p. The 23.0 MeV/u ^{14}C secondary beam was produced from a 60 MeV/u ^{18}O primary beam, separated by RIBLL1, and tracked onto a $(CH_2)_n$ (16.7 mg/cm^2) reaction target by three parallel plate avalanche chambers (PPACs). The beam intensity was about 3×10^4 particle per second (pps) with a purity of ~99.9%. The proton target was chosen considering the efficiency and precision of the threefold coincident measurement. The details of the experimental conditions and detector setups are given in the "Experimental set-up and detection performances" subsection in the "Methods". In addition to the aforementioned zero-degree detection system, the main advancement of the present measurement is to detect coincidentally all three final particles, ^{4}He+^{10}Be+^{1}H, by using a series of high-resolution silicon-strip detectors as depicted in Fig. 2[20,21]. This allows to deduce the beam-particle energy event-by-event, and thus to avoid the large energy spread of the projectile-fragmentation-type (PF-type) secondary beam which was responsible for the low resolution of the previous Q-value spectrum[30]. Another crucial improvement comes from the refined data analysis methods based on the properties of the multi-layer silicon-strip detectors, which leads to a significant increase in event statistics for the reconstructed resonant states[20,21]. These key techniques are described below.

Q-value spectrum. The decay ^{14}C $\rightarrow ^{10}$Be + α may end up at the ground or bound excited states of ^{10}Be, corresponding to different cluster separation thresholds E_{thr} or reaction Q-values. Since the measured relative energy E_r between the decay fragments ^{10}Be and α is related to the excitation energy E_x of
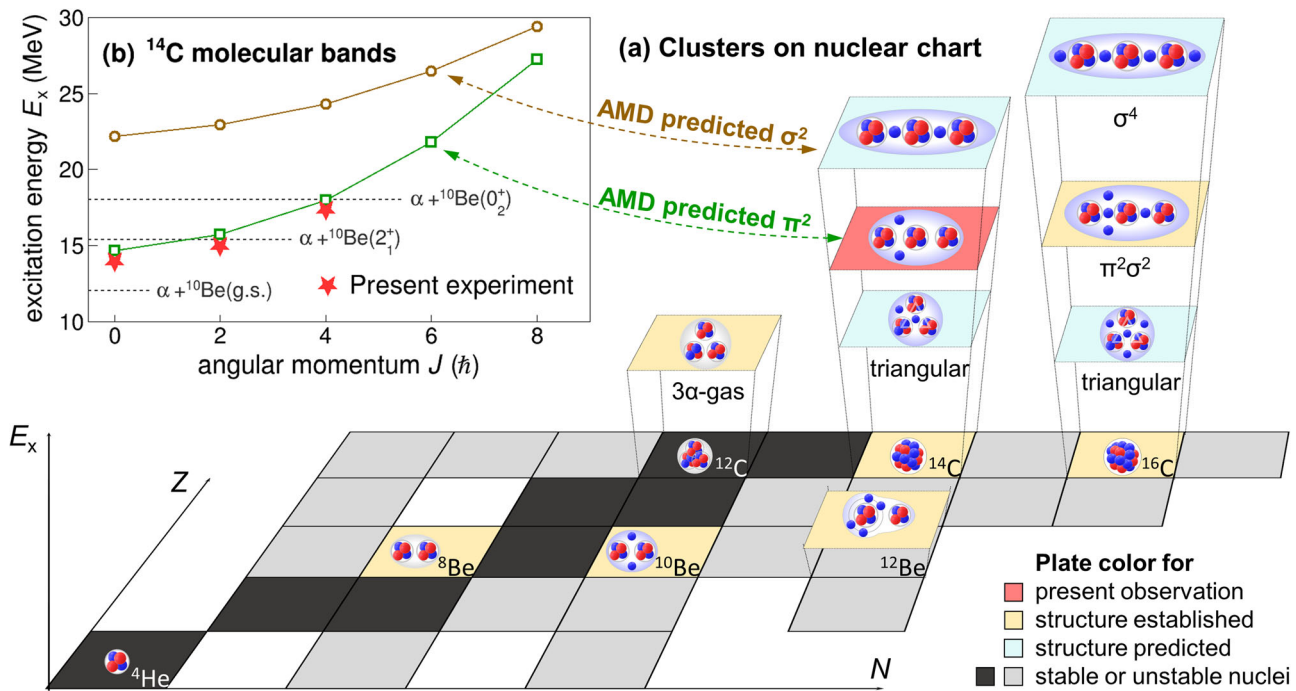
Fig. 1 Cluster-related structures in light even-even nuclei. a Illustration of nuclear chart (Z-proton number; N-neutron number) for cluster-related structures in light even-even nuclei, such as the 2-α-core beryllium systems and the 3-α-core carbon systems. The valence neutron configurations (π^2, σ^2, and $\pi^2\sigma^2$) for the triangle and chain-like structures in carbon isotopes are depicted according to the antisymmetrized molecular dynamics (AMD) calculations[14,15]. **b** Excitation energy-spin (E_x-J) systematics for the linear-chain molecular bands in ^{14}C, with the units of energy and spin represented by MeV and reduced Planck's constant $\hbar$, respectively. The error bars are not displayed as they are smaller in size compared to the data points (see the uncertainties for the excitation energies in Table 1 and the relevant explanations in the Excitation energy spectra subsection).
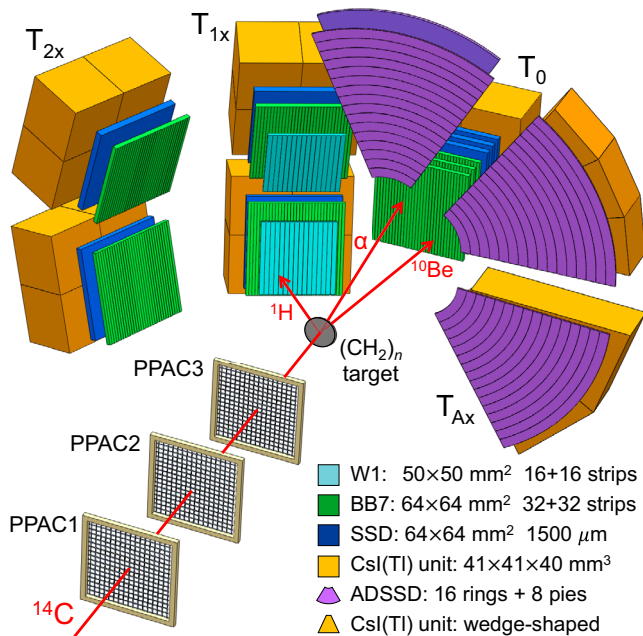

Fig. 2 Schematic view of the detection system. The beam particles ^{14}C (red line) are tracked by three parallel plate avalanche chambers (PPACs). x stands for up or down for the telescopes $T_{1x}(T_{2x})$, and equals to 1, 2 or 3 for the annular telescopes T_{Ax}. The telescopes are composed of double-sided silicon strip detectors (DSSDs) of W1 or BB7 type, annular double-sided silicon strip detectors (ADSSDs), large-size silicon detectors (SSDs), and CsI(Tl) scintillators. The final particles of interest are illustrated by the red arrows.

^{14}C through $E_x = E_r + E_{thr}$, it is an essential prerequisite to know E_{thr} (or Q-value) before converting the experimentally reconstructed E_r into the physically meaningful E_x[20,21]. Experimentally, the Q-value can be deduced from the energies of the final and initial particles:

$$Q = E_{Be} + E_{\alpha} + E_p - E_{beam}. \qquad (1)$$

Previously, the energy of the recoil particle (proton here) was determined via the momentum conservation between the beam and the final particles, resulting in low Q-value resolution due to the large energy spread of the PF-type secondary beam[30]. This problem has been overcome to a large extent in our recent work by further detecting the recoil particle and deducing event-by-event the energy of the beam particle via the momentum conservation[20,21]. This method is also employed in the present work and the achieved high-resolution of the Q-value spectrum is shown in Fig. 3a. As expected, two peaks at about −12.0 and −15.4 MeV can be clearly discriminated, corresponding to ^{10}Be in its ground state (g.s.) and first excited state (2^+_1, 3.37 MeV), respectively. In addition, the statistics of the coincidentally measured resonance-decay events have largely been improved by taking advantages of the multi-layer double-sided silicon-strip detectors (DSSDs)[20,21]. Previously, decay events with coincident signals on two adjacent strips were simply discarded to avoid mistaken events resulted from inter-strip hitting signals[19,30]. Recently, we have made extensive efforts to restore these close-by two-fragment events, by matching the energies from both sides of a single DSSD, tracking the hitting positions on neighboring DSSD layers and checking the location of the related energy pairs on the particle identification ($\Delta E - E$) spectra[20,21]. As a result, the number of accepted events for reconstructed resonance peaks, especially
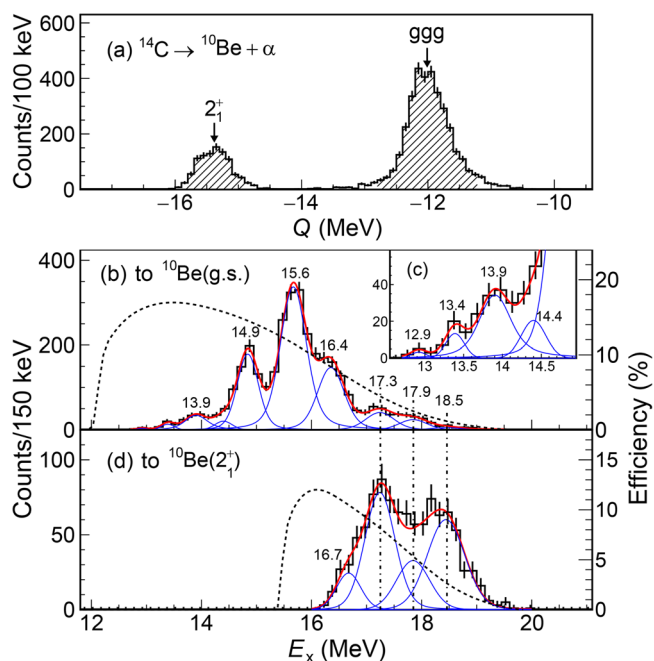
Fig. 3 Reaction Q-value and ^{14}C excitation energy spectra. a Q-value spectrum for the ^{1}H(^{14}C,^{14}C*→^{10}Be + α)p breakup reaction. **b–d** Excitation energy spectra of ^{14}C gated on the hatched areas in (**a**) for decaying into ^{10}Be(g.s.) (denoted as ggg) and ^{10}Be(2_1^+) with the decay threshold E_{thr} of 12.01 and 15.38 MeV, respectively. The insert (**c**) is an enlarged display of the near-threshold region of (**b**). Vertical error bars represent the corresponding statistical uncertainties (1 standard deviation). Each spectrum is fitted by the sum (thick red-solid line) of several resonance peaks (thin blue-solid lines). The black-dashed lines are the simulated detection efficiencies. The vertical dash-dotted lines are plotted to guide the eye for states decaying into both ^{10}Be(g.s.) and ^{10}Be(2_1^+).

Table 1 Resonant states in ^{14}C.

This work			Exp.[24–31]	AMD[14,15]	
E_x (MeV)	J^π	Γ_{tot} (keV)	E_x (MeV)	E_x (MeV)	J^π
12.9(1)[a]		30(10)	13.0, 13.1[a]		
13.4(1)[a]		30(10)			
13.9(1)[a]	0^+	150(30)	14.1[a]	14.64	0_4^+
14.4(1)[a]		30(20)	14.3[a]		
14.9(1)[a]	2^+	100(20)	14.7–14.9[a]	15.73	2_5^+
15.6(1)[a]	3^-	180(40)	15.5, 15.6[a,c]		
16.4(1)[a]		140(30)	16.4, 16.5[a,b]		
16.7(1)[b]		60(30)			
17.3(1)[a,b]	4^+	120(30)	17.3[a,b]	17.98	4_5^+
17.9(1)[a,b]		40(20)	17.8, 17.9[a,b]		
18.5(1)[a,b]		80(40)	18.4–18.8[a,b]		

Excitation energies (E_x), spin-parities (J^π) and total decay widths (Γ_{tot}) of the observed resonances in ^{14}C, compared to those from the previous experiments[24–31] and antisymmetrized molecular dynamics (AMD) calculations[14,15]. The uncertainties in the parentheses are explained in the "Excitation energy spectra" subsection.
[a]Decaying into ^{10}Be(g.s.).
[b]Decaying into ^{10}Be(2_1^+).
[c]Assigned a spin-parity of 3^-[28].

form)[20,21]. The peak positions and widths were initialized based on the experimental spectrum shape, the previously evidenced resonances and the consistency between the two decay paths. The presently extracted information on the resonances in ^{14}C is listed in Table 1, together with previously reported ones obtained from breakup reactions[24–31] and the latest antisymmetrized molecular dynamics (AMD) calculations[14,15]. The total uncertainties presented in the parentheses include both systematic and statistical uncertainties, and are dominated by the systematic ones (statistical ones) for the resonance energies (resonance widths). The systematic uncertainties were estimated based on the Monte Carlo simulation considering the realistic detection performances[24], while the statistical uncertainties were obtained from the fitting procedure. The statistically significant states at about 14.9, 15.6, and 16.4 MeV have been repeatedly observed in the present and previous breakup experiments[25–30], with the peak positions being consistent with each other within an uncertainty of 100 keV. In the lower energy region, several peaks appear with considerable statistics [Fig. 3c], owing to the background-free threefold coincident measurement and high detection efficiencies of the zero-degree telescope for decay fragments. The actually well-resolved small peak at about 12.9 MeV was marginally seen in two previous cluster-decay experiments[26,30], but a statistically meaningful analysis is still impossible due to a relatively low significance level (SL) of about 1.7σ (see the "Significance level analysis" subsection in the "Methods"). A peak at 13.4 MeV is evidenced with SL ≃ 3.5σ, which needs some further studies. The resonance at about 13.9 MeV was evidenced in two previous cluster-decay measurements[26,30], but now is observed with much higher statistics (SL > 8.0σ), enabling the subsequent angular correlation analysis. Just below the strong peak at 14.9 MeV, a component at about 14.4 MeV may exist (SL ≃ 3.8σ), which was already noticed in previous study[28]. At higher excitation energies, resonances at about 17.3, 17.9, and 18.5 MeV can be identified in both Fig. 3b, d, being also consistent with results of the previous breakup experiments[25,26,28–30].

those near the cluster-decay thresholds, has been significantly increased (see the "Experimental set-up and detection performances" subsection in the "Methods").

Excitation energy spectra. By gating on the Q-value peaks [Fig. 3a], the excitation energies of ^{14}C can be derived from the two decay fragments according to the standard invariant mass method[19–21], as shown in Fig. 3b–d. Monte-Carlo simulations were conducted to evaluate the detection efficiencies and resolutions, considering the energy and angular spread of the beam, the reaction position and energy loss uncertainties in the target, and the geometry and performances of the detectors. The application of the zero-degree telescope has enabled a high detection efficiency at excitation energies even very close to the decay threshold (dashed-lines in Fig. 3b, d). The resolution increases as $\sqrt{E_x - E_{thr}}$ and reaches ~400 keV (FWHM) at $E_x = 14.9$ MeV. The possible contaminant channel possessing the same final mass combination and thus the same Q-value is the triton transfer reaction ^{1}H(^{14}C,^{11}B*→^{10}Be + p)^{4}He. However, based on the Dalitz-plot analysis[37,38], this background channel was found to be negligible in comparison to the targeted inelastic excitation channel (see the "Contaminant channel analysis" subsection in the "Methods").

The excitation energy spectra presented in Fig. 3b, d were simultaneously fitted by using several resonance peaks of the Breit–Wigner form with an energy dependent width parameter[39] (see the "Approximate Breit–Wigner formula" subsection in the "Methods"), modified by the detection efficiencies and then convoluted with the energy-resolution functions (Gaussian

Spin-parity analyses. In previous breakup experiments, the spin-parities of the observed ^{14}C resonances were not well determined, except the one at 15.6 MeV for which 3^- was firmly assigned[28]. Presently achieved resolution and statistics allow to extract the spin-parities for up to four resonances in ^{14}C, using the mature angular correlation method[18,19,28,40–43]. The two polar angles involved here are θ^*, the center-of-mass scattering angle of the excited mother nucleus (^{14}C here) with respect to the beam axis, and ψ, the angle between the relative velocity vector of the two

decay fragments and the beam axis. The associated azimuthal angles are denoted as ϕ^* and χ, respectively. For spinless decay fragments, the angular correlation spectrum from a spin-J mother nucleus can be described by the square of a Legendre polynomial of order J, i.e., $|P_J(\cos\psi')|^2$[42,43] (see the "Angular correlation method and applications" subsection in the "Methods"). The projection $\psi' = \psi - \theta^*/a$ with $a = J/(l_i - J)$, with l_i (~5$\hbar$ here) being the dominant orbital angular momentum corresponding to the grazing trajectory in a peripheral reaction. The validity of this simple description requires the decay fragments ^{10}Be and ^{4}He to be in their 0^+ ground states [Fig. 3b, c] and emitting approximately in the reaction plane (in-plane correlation)[40,43]. The latter is assured by requiring $|\chi|\leq15°$ or $|\chi - 180°|\leq15°$. Other ranges of χ angle were also checked for consistency of the correlation pattern. For each bin of $\cos\psi'$, the excitation energy spectrum similar to Fig. 3b was built, and the similar fitting procedure was conducted to extract the yield for each resonance. Owing to the symmetry behavior of the experimental $\cos\psi'$ spectrum with respect to the conversion about $\psi = 90°$[41], and also the property of $|P_J(\cos\psi')|^2$ function, the angular correlation analysis has been performed against $|\cos\psi'|$ in order to have better statistical presentations[42,43]. The detection uncertainty (FWHM) in $|\cos\psi'|$ is less than 0.04 over the full range, mainly attributed to the angular resolution of the detectors and the uncertainty of the interaction position in the target. The behaviors of the obtained angular correlation spectra for the 15.6, 13.9, 14.9, and 17.3 MeV resonances [Fig. 4a–d] agree very well with the $|P_3|^2$, $|P_0|^2$, $|P_2|^2$ and $|P_4|^2$ functions, respectively. In contrast, other spin options would introduce out-of-phase descriptions with much larger $\tilde{\chi}^2$-values (see the "Angular correlation method and applications" subsection in the "Methods"). In the fitting of each spectrum, a constant background was added, which potentially resulted from the finite χ-angular range and the minor spin-flip effect induced by the none-zero spin of the proton target[41,42].

We note that the currently extracted 3^- spin-parity for the 15.6 MeV state [Fig. 4a] confirms the previous assignment that was also based on a clear angular correlation analysis[28]. This would validate our analyses for other three states at 13.9 MeV (0^+), 14.9 MeV (2^+), and 17.3 MeV (4^+) (Table 1). The resonance at ~16.4 MeV cannot be reasonably well described by a single $|P_x|^2$ function using the angular correlation method, possibly attributed to the mixing of different states in this peak (see the "Angular correlation method and applications" subsection in the "Methods"). It would be worth noting that the 15.07 MeV resonance reported in previous study[35] might have been strongly contaminated by states around 18.5 MeV as depicted in Fig. 3d, since the Q-value spectrum was unavailable there. As a consequence, the related spin assignment seems ambiguous.

The differential cross section of inelastic scattering or transfer reactions may provide complementary information on the spin-parities of the excited states, although its sensitivity is often lower than that of the angular correlation method, especially in the case of high excitation[19,44]. Based on the three-fold coincident events and using the momenta of the beam and the reconstructed ^{14}C*, we have obtained the differential cross section data as presented in Fig. 4e–h for the 15.6, 13.9, 14.9, and 17.3 MeV states. Here the resolution on θ^* is estimated to be ~2.2° (FWHM), mainly contributed from the uncertainties in determining the angles of the final particles and the reaction position in the target. Distorted-Wave Born Approximation (DWBA) calculations were performed using the code FRESCO[45], with the input optical potential parameters taken from the previous report[46]. The comparisons between the experimental data and the DWBA calculations favor the 3^-, 0^+, 2^+, and 4^+ assignments for the 15.6, 13.9, 14.9, and 17.3 MeV states, respectively. This further supports the spin assignments from the angular correlation analyses.
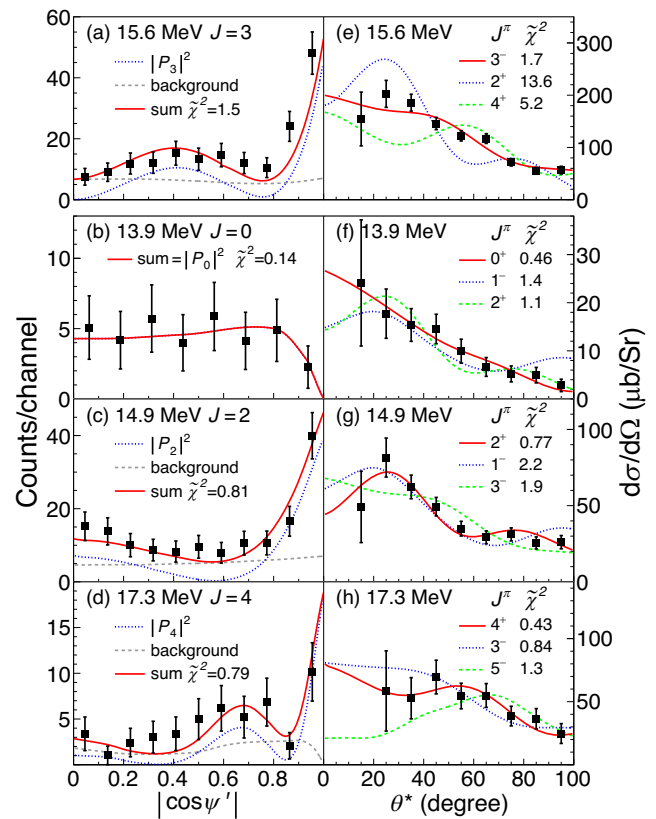
Fig. 4 Angular correlation and differential cross section spectra. a–d: Experimental angular correlation spectra (black squares) for the 15.6, 13.9, 14.9, and 17.3 MeV states, each compared with the sum (red-solid line) of a Legendre polynomial $|P_J(\cos\psi')|^2$ of order $J = 3$, 0, 2, or 4 (blue-dotted line), respectively, and a constant background (gray-dashed line). **e–h** show the corresponding differential cross sections (black squares), fitted with distorted-Wave Born Approximation (DWBA) calculations under different spin-parity assumptions (lines). All curves have been corrected by simulated efficiencies and resolutions. The error bars show the statistical uncertainties (one standard deviation). The corresponding reduced $\tilde{\chi}^2$ are also indicated.

Comparison to the AMD calculations. The latest AMD approach[14,15] has predicted the positive parity linear-chain structure in ^{14}C. The calculation has correctly reproduced the cluster-separation threshold and then proposed the first three members of the π-bond molecular rotational band at 14.64 MeV (0_4^+), 15.73 MeV (2_5^+) and 17.98 MeV (4_5^+), as listed in Table 1. The currently observed 13.9 MeV (0^+), 14.9 MeV (2^+) and 17.3 MeV (4^+) states correspond to these members, as shown in Fig. 1b. The shifts between the data and the predictions, with an average value of 0.75 MeV, may be attributed to an offset related to the effective interaction used in the calculation, which has already introduced a similar shift to the low-lying 2_1^+ state of ^{14}C[14]. As the 17.3 MeV resonance decays strongly to the first excited state of ^{10}Be, we can further check its structure property using the selective decay-path method, which has been proposed and successfully applied in recent works[16,20,21]. The presently extracted ratio of the decay probabilities from the 17.3 MeV state of ^{14}C into the ground and first excited states of ^{10}Be is 1.1 ± 0.1 (statistical error, 1 standard deviation), in reasonable agreement with the corresponding decay ratio of about $149/118 = 1.26$ (channel radius $a = 5.2$ fm) predicted by the AMD model[14,15]. Considering the close resemblance in excitation energies and the corresponding spin-parity assignments, together with the

selective decay paths, we may allocate the observed 13.9, 14.9 and 17.3 MeV resonant states as the 0^+, 2^+, and 4^+ members, respectively, of the predicted π-bond positive-parity linear-chain molecular band of ^{14}C (Fig. 1b). From the experimental data, a $\hbar^2/2\mathfrak{I}$ value of about 170 keV can be deduced, with $\mathfrak{I}$ being the moment of inertia. This large moment of inertia is comparable to that predicted by the AMD model ($\hbar^2/2\mathfrak{I} = 179$ keV) for the π-bond linear-chain molecular band, corresponding to a quadrupole deformation parameter β of about 1.0[14,15].

Conclusions

In conclusion, we have presented a breakup experiment to search for the exotic linear-chain structure in ^{14}C. Owing to the threefold coincident detection of all final particles ^{4}He$+^{10}$Be$+^1$H with high efficiencies, a high resolution on the Q-value spectrum was achieved, providing the basis for the unambiguous spin and decay-path analyses. The near-threshold resonance at 13.9(1) MeV was firmly observed, together with the extracted spin-parity of 0^+. The spin-parities of the 14.9(1) and 17.3(1) MeV states are determined to be 2^+ and 4^+ based on the angular correlation and characteristic decay-paths analyses. These three resonances correspond to the first three members of the predicted π-bond linear-chain molecular rotational band in ^{14}C and strongly evidence the emergence of the chain structure starting from ^{14}C. The presented methods and results encourage further studies of the chain configuration in heavier neutron-rich nuclei and should also be of value for cluster-structure investigations in other non-nuclear systems.

Methods

Experimental set-up and detection performances. A schematic layout of the detection system is given in Fig. 2. The T_0, T_{1x}, and T_{2x} telescopes were centered at 0°, 30.8°, and 68.5°, respectively, relative to the beam direction, and all located at a distance of about 170.0 mm downstream from the target. T_0 comprised three 1000-μm-thick double-sided silicon strip detectors (DSSDs) of BB7 type, three large-size silicon detectors (SSDs), and a 2 × 2 CsI(Tl) scintillator array. It accepted almost 100% of the two forward moving fragments ^{10}Be and α from the decay of near-threshold resonances in ^{14}C owing to the inverse kinematics[20,21,30]. T_{1x} consisted of two DSSDs (50-μm W1 and 300-μm BB7), one SSD and a 2 × 2 CsI(Tl) array. T_{2x} had only one DSSD (65-μm BB7) followed by one SSD and a CsI(Tl) array as for T_{1x}. T_{Ax} was composed of a set of annular double-sided silicon strip detectors (ADSSDs) backed by the wedge-shaped CsI(Tl) scintillators. The details of T_{Ax} can be found in our previous publication[47]. T_{1x}, T_{2x} and T_{Ax} telescopes were arranged in a compact configuration in order to cover larger solid angles for the recoil proton detection.

Timing signals were collected from each strip of the silicon detectors and the beam monitoring scintillators, which were used to suppress the event-mixing background[20,21,43]. The overall energy match for different strips in one DSSD was achieved according to the self-uniform calibration method[48]. And then particles produced from the nuclear reactions on the detector layers, but not on the physics target, were largely eliminated by the tracking analysis combining hit positions on the target and on several neighboring DSSD layers[20,21,30,43]. The absolute energy calibration of each silicon-detector was accomplished by comparing the experimental particle identification curves in Fig. 5 with those calculated using energy-loss tables[49], and further checked by using a combination of α-particle sources. The characteristic energy resolutions of the present silicon detectors are about 1% for the 5.486-MeV α particles emitted from the ^{241}Am source. The energy calibration for CsI(Tl) scintillators was realized by the procedures described in our previous study[47], taking into account the non-linearity and particle-dependence of the light output. Thanks to the high resolutions on the energy and
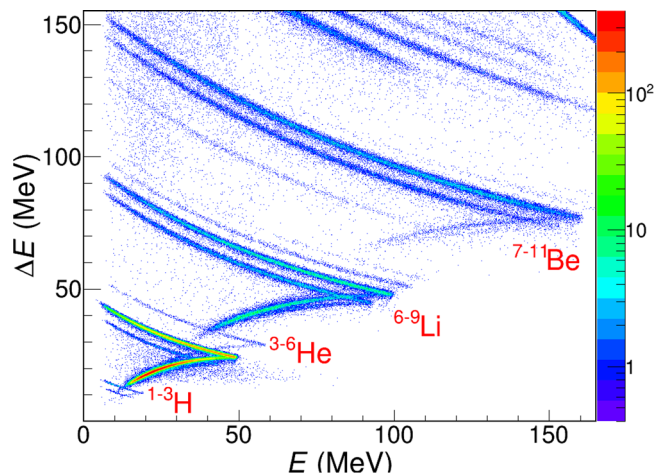
Fig. 5 Particle identification spectrum. The spectrum was measured by the first two layers of the T_0 telescope using the $\Delta E - E$ method. Note that ^{5}He and ^{8}Be are missing from the observed bands as expected.
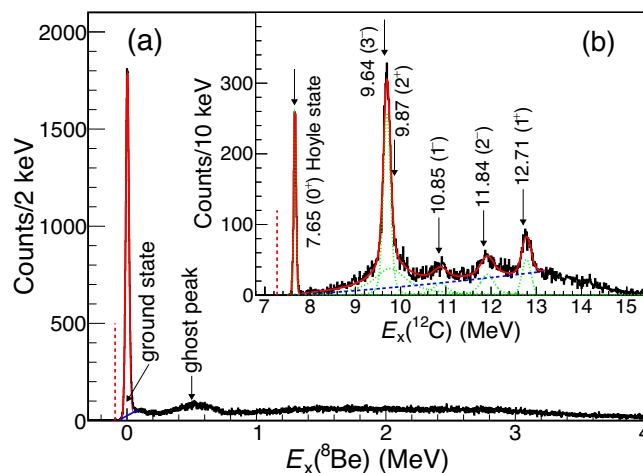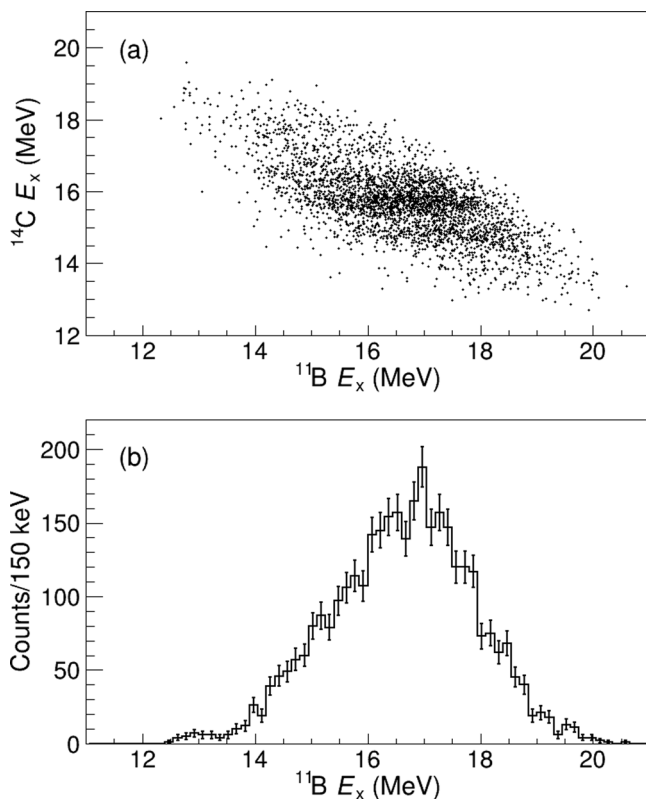

Fig. 6 Excitation energy spectra from the multi-α events. Excitation energy spectra of **a** ^{8}Be from 2-α and **b** ^{12}C from 3-α coincident detection. Each spectrum is fitted by the sum (red-solid line) of several resonance peaks (green-dotted lines) and a smooth background (blue-dashed line). The vertical red-dashed lines in (**a**) and (**b**) stand for the 2-α and 3-α decay thresholds of ^{8}Be (−91.8 keV) and ^{12}C (7.27 MeV), respectively. Arrows indicate the position of known states. The error bars are not displayed as they are smaller in size compared to the data points, which is attributed to the high statistics within each bin.

position measurements, isotopes from hydrogen to beryllium were unambiguously identified based on the standard energy loss versus residual energy ($\Delta E - E$) technique, as exhibited in Fig. 5.

The detection and calibration were validated by reconstructing the known ^{8}Be and ^{12}C resonances with the coincidentally detected two- and three-α particles, respectively[21,42], as displayed in Fig. 6. Using the 2-α events, we see in Fig. 6a the ground peak of ^{8}Be at about 91.8 keV above the α-α decay threshold. The width (FWHM) of this peak is only 30 keV and mainly attributed to the detection resolutions, since the intrinsic width of this state ($\Gamma = 5.57$ eV) can be neglected. The ghost peak, resulting from the α decay following the neutron emission of the second excited state of ^{9}Be (2.43 MeV, $5/2^-$), was also identified at around 0.5 MeV in previous studies[21,42]. Using the 3-α events, it appears the strongly populated Hoyle state (7.654 MeV, 0^+_2, $\Gamma = 9.3$ keV) of ^{12}C[23] with the extracted energy resolution (FWHM) of only 63 keV, as demonstrated in Fig. 6b. In addition, the

reconstructed states of ^{12}C at higher energies are in good agreement with the ENSDF[50] data of nuclear levels. The extracted energy resolution (FWHM) increases as $\sqrt{E_x - E_{thr}}$, with E_{thr} being the 3-α decay threshold of ^{12}C). This resolution is about 156 keV for the most prominent 9.64 MeV (3_1^-, $\Gamma = 42$ keV) state.

Contaminant channel analysis. There exists one possible contaminant channel, namely, ^{1}H(^{14}C,^{11}B*$\rightarrow$^{10}Be + p)^{4}He, which possesses the same mass combination for final particles and thus the same Q-value as for the targeted inelastic excitation channel. However, this channel tends to emit the decay proton into the forward angle and the recoiling ^{4}He into a large angle. This is just in contrast to the targeted inelastic scattering and decay process and, therefore, not favored by the experimental setup and particle selection strategy. To evaluate the possible contamination of this transfer reaction channel, we used the tree-fold coincident events to build a Dalitz-type plot, namely the ^{10}Be + ^{4}He reconstructed ^{14}C excitation energy versus the ^{10}Be + p reconstructed ^{11}B excitation energy, as displayed in Fig. 7(a). From the figure, clear band structures can be observed for certain ^{14}C-E_x values but not at all for ^{11}B-E_x. The projection onto the one-dimensional spectrum for ^{11}B excitation energy (Fig. 7b) is completely structureless, indicating a low probability of this background channel in the actually accepted three-fold coincident data.

Approximate Breit–Wigner formula. The full Breit–Wigner form is given by:

$$f(E_r; E_0, R, \gamma) = \frac{\Gamma_l(E_r; R, \gamma)}{[E_r - E_{r0} - \Delta_l(E_r; E_{r0}, \gamma)]^2 + \Gamma_l^2(E_r; R, \gamma)/4},$$

(2)

where E_r and E_{r0} are the relative energy and the central relative energy of a resonance reconstructed from the interested decay channel, respectively. The energy dependence of the resonance width, Γ_l, is given by $\Gamma_l(E_r; R, \gamma) = 2P_l(E_r; R)\gamma^2$, where γ^2 and $P_l(E_r; R)$ are the reduced width and the penetration factor, respectively. $P_l(E_r; R)$ can be calculated from the regular and irregular Coulomb wave functions, $F_l(kR)$ and $G_l(kR)$,
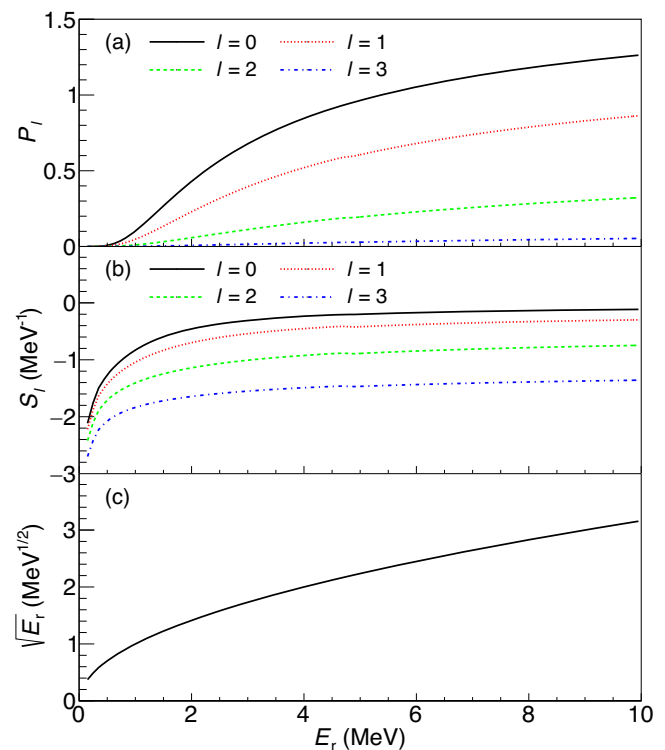
$$P_l(E_r; R) = \frac{kR}{F_l(kR)^2 + G_l(kR)^2},$$

(3)

where R is the channel radius and $k = \sqrt{2\mu E_r}$ the wave number. The energy dependence of the resonance shift, $\Delta_l(E_r; E_{r0}, \gamma)$, is determined from the shift function $S_l(E_r)$,

$$\Delta_l(E_r; E_{r0}, \gamma) = -[S_l(E_r) - B]\gamma^2,$$

(4)

where the boundary condition B is chosen such that $\Delta_l(E_r = E_{r0}) = 0$. This complete (but complicated) Breit-Wigner formula is commonly employed to describe an individual resonant peak[19,51] or multiple resonant peaks with well-known spin-parities[19,52].

In the case of multiple unknown resonances, some kind of approximated Breit-Wigner forms have been frequently applied. In Fig. 8a, b, we plot the penetration factors $P_l(E_r; R)$ and shift functions $S_l(E_r)$ for various angular momenta l. For states at relatively high E_r and with relatively narrow width, as the cases observed in our work (see Table 1), it is reasonable to keep the penetration factor P_l and the shift function S_l as constants with

Fig. 7 Dalitz-plot for the contamination channel. a Dalitz-type plot for the reconstructed ^{14}C excitation energy versus the reconstructed ^{11}B excitation energy; **b** the projection of (**a**) onto one-dimensional spectrum for ^{11}B excitation energy. Vertical error bars represent the corresponding statistical uncertainties (1 standard deviation).

Fig. 8 Behaviors of various components of the Breit–Wigner formula. a The penetration factors $P_l(E_r; R)$ and **b** the shift functions $S_l(E_r)$ for various angular momenta l. **c** The function $\sqrt{E_r}$.

respect to E_r for a specific resonance. According to the definition of the boundary condition B, the resonance shift Δ_l now becomes zero, and the Breit–Wigner formula can be simplified as:

$$f(E_r; E_{r0}, \Gamma) = \frac{\Gamma}{[E_r - E_{r0}]^2 + \Gamma^2/4}. \quad (5)$$

This simple form has been widely used in many cases[32,53,54].

In order to still keep an asymmetric shape of the Breit–Wigner form, another approximation has been usually adopted. The penetration factor $P_l(E_r; R)$ can be expressed as:

$$P_l(E_r; R) = \frac{\sqrt{2\mu}R}{F_l(kR)^2 + G_l(kR)^2} \sqrt{E_r} = g_l' \sqrt{E_r}, \quad (6)$$

with $g_l' = \sqrt{2\mu}R/(F_l(kR)^2 + G_l(kR)^2)$. By comparing Fig. 8a with Fig. 8c, it is clear that the energy-dependent behavior of $P_l(E_r; R)$ is essentially represented by $\sqrt{E_r}$ and the g_l' can then be approximated as a constant for each resonant state, namely $\Gamma \sim g\sqrt{E_r}$. We note that the g factor here is a constant with respect to E_r but dependent on l and γ^2 for each resonant state. This approximated formula has been used in many other cases[39,55]. Due to the quite complicated resonance structure in our case, we have adopted this method, and the fitting-resulted g factors are 0.109(22), 0.059(12), 0.095(21) and 0.052(13) MeV$^{1/2}$, for the resonances at 13.9, 14.9, 15.6, and 17.3 MeV, respectively, corresponding to the $\Gamma(E_{r0})$ values listed in Table 1 of the manuscript.

Significance-level analysis. The significance level for each state below 14.9 MeV, which possesses a relatively low statistics, was estimated. For states determined by the fitting procedure, the usual method is to compare the likelihood L of the fits with (L_{H1}) and without (L_{H0}) including the targeted state[56]. The difference of log-likelihood values $\Delta(L)$ can thus be translated into a p value, corresponding to a number of σ, as a measure of the significance level. For the states at 12.9, 13.4, and 14.4 MeV, we obtained $\Delta(L) = 3.1$, 12.2, and 14.2 (Δndf = 1), leading to significance levels of 1.7σ, 3.5σ, and 3.8σ, respectively. For the statistically more significant state at 13.9 MeV, the obtained value is $\Delta(\ln L) = 93$ (Δndf = 1), leading to a significance level higher than 8σ.

Angular correlation method and applications. For a sequential reaction-decay process a(A, B* → c+C)b, the intermediate resonant particle B* may decay into, for instance, two spin-zero fragments. The angular correlation of the latter is a sensitive probe of the spin of the mother nucleus B*[40,57,58]. In a spherical coordinate system with its z-axis pointing to the beam direction, the correlation function can be parameterized in terms of four angles. These are the center-of-mass (c.m.) scattering polar angle θ^* and azimuthal angle ϕ^* of the resonant particle B*, and the polar angle ψ and azimuthal angle χ of the relative velocity vector of the two fragments. Both polar angles, θ^* and ψ, are with respective to the beam direction. The azimuthal angle ϕ takes a value of 0° (or 180°) in the horizontal plane defined by the center positions of the detectors placed at the opposite sides of the beam (the chamber plane or the detection plane). Another azimuthal angle χ is defined as 0° (or 180°) in the reaction plane fixed by the beam axis and the reaction product B*.

When the azimuthal angle χ was restricted to 0° or 180° (the so-called in-plane correlation), the angular correlation in the θ^*-ψ plane appears as the ridge structures associated with the spin of the mother nucleus[40]. At relatively small θ^* angles, the structure is characterized by the locus $\theta^* = a\psi$ in the double differential cross sections, where a is a constant for the slope of the ridge and nearly inversely proportional to the spin of the resonant state B*. Within the strong absorption model, a is related to the orbital angular moment l_i of the dominant partial wave in the entrance
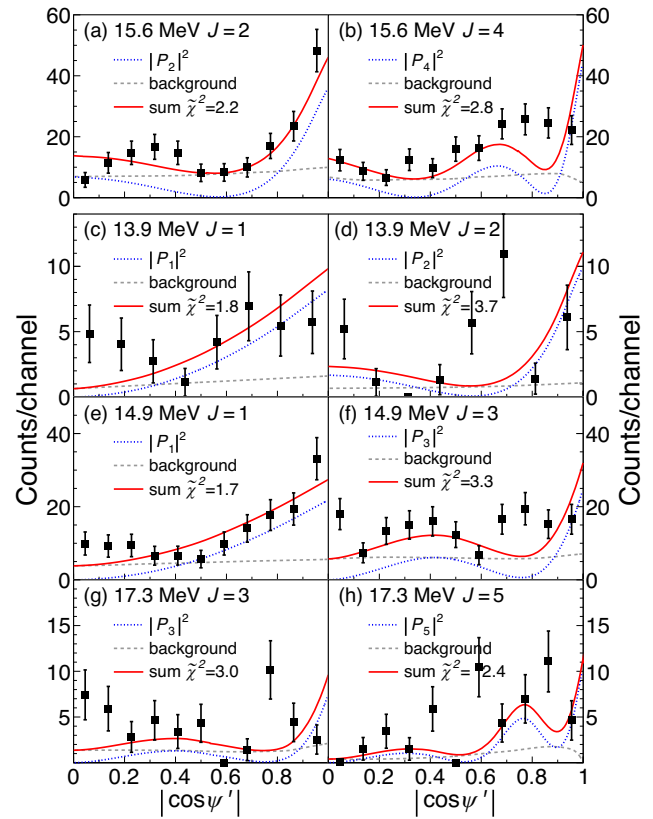

Fig. 9 Additional angular correlation analyses. The paired figures (**a**, **b**), (**c**, **d**), (**e**, **f**), and (**g**, **h**) present angular correlation spectra (black squares) for the 15.6, 13.9, 14.9, and 17.3 MeV states, respectively, with each pair compared to the sum (red-solid line) of a Legendre polynomial $|P_J(\cos \psi')|^2$ of order J (blue-dotted line) and the background (gray-dashed line). For each figure, the projected data with spin-J assumption different from that adopted in Fig. 4 is compared with the corresponding Legendre polynomial. All curves have been corrected by simulated efficiencies and resolutions. The error bars represent the statistical uncertainties (one standard deviation). The corresponding reduced $\widetilde{\chi}^2$ are also indicated.

channel by $a = \frac{J}{l_i - J}$, with J being the spin of B*. l_i can be evaluated simply from $l_i = r_0(A_p^{1/3} + A_t^{1/3})\sqrt{2\mu E_{c.m.}}$, where A_p and A_t are the mass numbers of the beam and target nucleus, respectively, μ the reduced mass and $E_{c.m.}$ the center-of-mass energy[57]. If the resonant nucleus is emitted to angles close to $\theta^* = 0°$, the projected correlation function $W(\psi')$ is simply proportional to the square of the Legendre polynomial of order J, namely $|P_J(\cos(\psi))|^2$. This method has been frequently applied in the literature[28,42,43,58].

We present here in Fig. 9 the comparison of the angular correlation data with $|P_J(\cos \psi')|^2$ functions for spin-J values other than those adopted in Fig. 4. It should be noted that each angular correlation spectrum as a function of ψ' comes from the projection of the $\theta^* - \psi$ two-dimensional distribution according to $\psi' = \psi - \theta^*(l_i - J)/J$. It means that the projected data and the applied $|P_J|^2$ function must follow the same J in order to be comparable. This also explains why the angular correlation spectra for the same resonance but projected onto different J values may look different, and why they should be plotted on separate graphs to avoid confusion. Figure 9 displays the angular correlation spectra for the 15.6, 13.9, 14.9, and 17.3 MeV states, each compared with two Legendre polynomials of orders adjacent to those adopted in Fig. 4a–d. In the manuscript, we take the 15.6
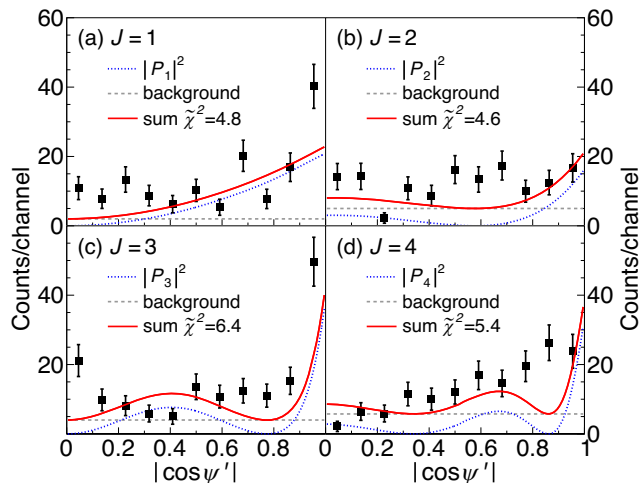
Fig. 10 Angular correlation spectra of the 16.4 MeV state. Angular correlation spectra (black squares) of the 16.4 MeV state under the spin-J assumption of 1 (**a**), 2 (**b**), 3 (**c**) and 4 (**d**), each compared to the sum (red-solid line) of the corresponding Legendre polynomial $|P_J(\cos\psi')|^2$ of order J (blue-dotted line) and the background (gray-dashed line). All curves have been corrected by the simulated efficiencies. The error bars represent the statistical uncertainties (1 standard deviation). The corresponding reduced $\widetilde{\chi}^2$ are also indicated.

MeV state [Fig. 4a] as a reference to be compare with the previously well-established spin-parity assignment of 3^-[28]. It is evident from Fig. 9a, b that $J = 2$ or 4 can be ruled out for this state due to the out-of-phase behavior between the data and the corresponding $|P_J|^2$ function, and also due to the much larger $\widetilde{\chi}^2$-values. For the newly determined 13.9 MeV (0^+) state [Fig. 4b], the 1^- or 2^+ possibilities can also be unambiguously eliminated, as demonstrated by Fig. 9c, d. We note that, if the applied spin is incorrect, the projected data may even be scattered without reasonable shape, as exhibited in Fig. 9d. Finally, the comparison between Fig. 4c and Fig. 9e–f, or between Fig. 4d and Fig. 9g–h, also gives clear support to the spin-parity assignments of 2^+ or 4^+ for the 14.9 or 17.3 MeV state, respectively.

In Fig. 10, we plot the comparisons between the angular correlation data and the functions $|P_J(\cos\psi')|^2$ ($J = 1, 2, 3, 4$) for the 16.4 MeV peak in Fig. 3b. We note that the projected data is also related to the assumed angular momentum J. Observably, due to the out-of-phase behavior between the data and the corresponding $|P_J|^2$ functions, as well as significantly larger $\widetilde{\chi}^2$-values, $J = 1, 2, 3$, or 4 can be ruled out for this excitation state. By referring to Fig. 3d, it is quite possible that the actual 16.4 MeV peak in Fig. 3b may contain some contribution from the 16.7 MeV state. As a test, we have attempted to fit the spectrum in Fig. 3b by incorporating a peak component centered at 16.7 MeV. This would result in a narrower width for the 16.4 MeV state, but still adhere to the simulated energy resolution. Since this mixture cannot be clearly determined from the present measurement and also does not affect the main conclusion of the present studies, we will keep the results as presented in Table 1.

Data availability
All data that support the plots within this paper and other findings of this study are available from the corresponding author upon reasonable request.

Code availability
The code used during the study is available from the corresponding author upon reasonable request.

References
1. Haxel, O., Jensen, J. H. D. & Suess, H. E. On the "magic numbers" in nuclear structure. *Phys. Rev.* **75**, 1766 (1949).
2. Mayer, M. G. On closed shells in nuclei. II. *Phys. Rev.* **75**, 1969 (1949).
3. von Oertzen, W., Freer, M. & Kanada-En'yo, Y. Nuclear clusters and nuclear molecules. *Phys. Rep.* **432**, 43–113 (2006).
4. Ikeda, K., Takigawa, N. & Horiuchi, H. The systematic structure-change into the molecule-like structures in the self-conjugate 4n nuclei. *Prog. Theor. Phys. Suppl.* **E68**, 464–475 (1968).
5. Horiuchi, H., Ikeda, K. & Kato, K. Recent developments in nuclear cluster physics. *Prog. Theor. Phys. Suppl.* **192**, 1–238 (2012).
6. Funaki, Y., Horiuchi, H. & Tohsaki, A. Cluster models from rgm to alpha condensation and beyond. *Prog. Part. Nucl. Phys.* **82**, 78–132 (2015).
7. Liu, Y. & Ye, Y. L. Nuclear clustering in light neutron-rich nuclei. *Nucl. Sci. Tech.* **29**, 1–16 (2018).
8. Genzel, R., Eisenhauer, F. & GillessenMayer, S. The Galactic Center massive black hole and nuclear star cluster. *Rev. Mod. Phys.* **82**, 3121 (2010).
9. Chen, H. X., Chen, W., Liu, X. & Zhu, S. L. The hidden-charm pentaquark and tetraquark states. *Phys. Rep.* **639**, 1 (2016).
10. Tohsaki, A., Horiuchi, H., Schuck, P. & Röpke, G. Alpha cluster condensation in ^{12}C and ^{16}O. *Phys. Rev. Lett.* **87**, 192501 (2001).
11. Hagino, K., Sagawa, H., Carbonell, J. & Schuck, P. Coexistence of bcs- and bec-like pair structures in halo nuclei. *Phys. Rev. Lett.* **99**, 022506 (2007).
12. Kobayashi, F. & Kanada-En'yo, Y. Dineutron formation and breaking in ^{8}He. *Phys. Rev. C* **88**, 034321 (2013).
13. Suhara, T. & Kanada-En'yo, Y. Cluster structures of excited states in ^{14}C. *Phys. Rev. C* **82**, 044301 (2010).
14. Baba, T. & Kimura, M. Structure and decay pattern of the linear-chain state in ^{14}C. *Phys. Rev. C* **94**, 044303 (2016).
15. Baba, T. & Kimura, M. Three-body decay of linear-chain states in ^{14}C. *Phys. Rev. C* **95**, 064318 (2017).
16. Baba, T. & Kimura, M. Characteristic α and ^{6}He decays of linear-chain structures in ^{16}C. *Phys. Rev. C* **97**, 054315 (2018).
17. Freer, M., Horiuchi, H., Kanada-En'yo, Y., Lee, D. & Meißner, U. G. Microscopic clustering in light nuclei. *Rev. Mod. Phys.* **90**, 035004 (2018).
18. Freer, M. et al. α: 2n: α Molecular Band in ^{10}Be. *Phys. Rev. Lett.* **96**, 042501 (2006).
19. Yang, Z. H. et al. Observation of enhanced monopole strength and clustering in ^{12}Be. *Phys. Rev. Lett.* **112**, 162501 (2014).
20. Liu, Y. et al. Positive-parity linear-chain molecular band in ^{16}C. *Phys. Rev. Lett.* **124**, 192501 (2020).
21. Han, J. X. et al. Observation of the $\pi^2\sigma^2$-bond linear-chain molecular structure in ^{16}C. *Phys. Rev. C* **105**, 044302 (2022).
22. Zhao, P. W., Itagaki, N. & Meng, J. Rod-shaped nuclei at extreme spin and isospin. *Phys. Rev. Lett.* **115**, 022501 (2015).
23. Morinaga, H. Interpretation of some of the excited states of 4n self-conjugate nuclei. *Phys. Rev* **101**, 254 (1956).
24. Li, J. et al. Selective decay from a candidate of the σ-bond linear-chain state in ^{14}C. *Phys. Rev. C* **95**, 021303(R) (2017).
25. Soić, N. et al. ^{4}He decay of excited states in ^{14}C. *Phys. Rev. C* **68**, 014321 (2003).
26. Milin, M. et al. The ^{6}He scattering and reactions on ^{12}C and cluster states of ^{14}C. *Nucl. Phys. A* **730**, 285–298 (2004).
27. Price, D. L. et al. Alpha-decay of excited states in ^{13}C and ^{14}C. *Nucl. Phys. A* **765**, 263–276 (2006).
28. Price, D. L. et al. α decay of excited states in ^{14}C. *Phys. Rev. C* **75**, 014305(R) (2007).
29. Haigh, P. J. et al. Measurement of α and neutron decay widths of excited states of ^{14}C. *Phys. Rev. C* **78**, 014319 (2008).
30. Zang, H. L. et al. Investigation of the near-threshold cluster resonance in ^{14}C. *Chin. Phys. C* **42**, 074003 (2018).
31. Tian, Z. Y. et al. Cluster decay of the high-lying excited states in ^{14}C. *Chin. Phys. C* **40**, 111001 (2016).
32. Yu, H. Z. et al. Novel evidence for the σ-bond linear-chain molecular structure in ^{14}C. *Chin. Phys. C* **45**, 084002 (2021).
33. Freer, M. et al. Resonances in ^{14}C observed in the ^{4}He(^{10}Be, α)^{10}Be reaction. *Phys. Rev. C* **90**, 054324 (2014).
34. Fritsch, A. et al. One-dimensionality in atomic nuclei: a candidate for linear-chain α clustering in ^{14}C. *Phys. Rev. C* **93**, 014321 (2016).
35. Yamaguchi, H. et al. Experimental investigation of a linear-chain structure in the nucleus ^{14}C. *Phys. Lett. B* **766**, 11–16 (2017).
36. Sun, Z., Zhan, W. L., Guo, Z. Y., Xiao, G. & Li, J. X. Ribll, the radioactive ion beam line in lanzhou. *Nucl. Instrum. Methods Phys. Res. Sect. A* **503**, 496–503 (2003).

37. Feng, J. et al. Enhanced monopole transition strength from the cluster decay of ^{13}C. *Sci. Chin. Phys. Mech. Astron.* **62**, 1–7 (2019).

38. Dalitz, R. H. Cxii. On the analysis of τ-meson data and the nature of the τ-meson. *Lond. Edinb. Dubl. Phil. Mag. J. Sci.* **44**, 1068–1080 (1953).

39. Tanaka, J. et al. Halo-induced large enhancement of soft dipole excitation of ^{11}Li observed via proton inelastic scattering. *Phys. Lett. B* **774**, 268–272 (2017).

40. Freer, M. The analysis of angular correlations in breakup reactions: the effect of coordinate geometries. *Nucl. Instrum. Methods Phys. Res. Sect. A* **383**, 463–472 (1996).

41. Curtis, N. et al. Decay angular correlations and spectroscopy for ^{10}Be$^* \rightarrow {}^4$He + ^{6}He. *Phys. Rev. C* **64**, 044604 (2001).

42. Dell'Aquila, D. et al. New experimental investigation of the structure of ^{10}Be and ^{16}C by means of intermediate-energy sequential breakup. *Phys. Rev. C* **93**, 024611 (2016).

43. Yang, B. et al. Investigation of the ^{14}C + α molecular configuration in ^{18}O by means of transfer and sequential decay reaction. *Phys. Rev. C* **99**, 064315 (2019).

44. Satchler, G. R. Isospin and macroscopic models for the excitation of giant resonances and other collective states. *Nucl. Phys. A* **472**, 215–236 (1987).

45. Thompson, I. J. Coupled reaction channels calculations in nuclear physics. *Comp. Phys. Rep.* **7**, 167–212 (1988).

46. Menet, J. J. H., Gross, E. E., Malanify, J. J. & Zucker, A. Total-reaction-cross-section measurements for 30-60-MeV protons and the imaginary optical potential. *Phys. Rev. C* **4**, 1114–1129 (1971).

47. Li, G. et al. Property investigation of the wedge-shaped CsI(Tl) crystals for a charged-particle telescope. *Nucl. Instrum. Methods Phys. Res. Sect. A* **1013**, 165637 (2021).

48. Qiao, R. et al. A new uniform calibration method for double-sided silicon strip detectors. *IEEE Trans. Nucl. Sci.* **61**, 596–601 (2014).

49. Ziegler, J. F., Ziegler, M. D. & Biersack, J. P. Srim – the stopping and range of ions in matter (2010). *Nucl. Instrum. Methods Phys. Res. Sect. B* **268**, 1818–1823 (2010).

50. National Nuclear Data Center. Evaluated Nuclear Structure Data File (ENSDF). https://www.nndc.bnl.gov/ensdf/ (2023).

51. Cao, Z. X. et al. Recoil proton tagged knockout reaction for ^{8}He. *Phys. Lett. B* **707**, 46–51 (2012).

52. Bohlen, H. G. et al. Spectroscopy of particle-hole states of ^{16}C. *Phys. Rev. C* **68**, 054606 (2003).

53. Wang, D. X. et al. α-Cluster decay from 24Mg resonances produced in the ^{12}C(^{16}O,^{24}Mg)α reaction. *Chin. Phys. C* **47**, 014001 (2023).

54. Liu, W. et al. s- and d-wave intruder strengths in ^{13}B$_{g.s.}$ via the ^{1}H(^{13}B, d)^{12}B reaction. *Phys. Rev. C* **104**, 064605 (2021).

55. Liu, W. et al. New investigation of low-lying states in ^{12}Be via a ^{2}H(^{13}B,^{3}He) reaction. *Phys. Rev. C* **105**, 034613 (2022).

56. Tanabashi, M. et al. Review of particle physics. *Phys. Rev. D* **98**, 030001 (2018).

57. Rae, W. D. M. & Bhowmik, R. K. Reaction mechanism and spin information in the sequential breakup of ^{18}O at 82 MeV. *Nucl. Phys. A* **420**, 320–350 (1984).

58. Yang, B. et al. Spin determination by in-plane angular correlation analysis in various coordinate systems. *Chin. Phys. C* **43**, 084001 (2019).

Acknowledgements

Author contributions

Y.Y., J.H., and J. Lou designed and led the experiment. J.H., B.Y., Y.L., S.B., K.M., J.C., G.L., Z.H., H.Y., Z.T., L.Y., S.W., L.T., W.L., Y.J., Jingjing Li, Dongxi Wang, S.H., Y.C., W.P., K.W., H.H., Zhihuan Li, Y.Y., J.W., J.M., H.Y., P.M., S.X., Z.B., S.J., F.D., Y.S., L.H., Y.L., Junwei Li, S.Z., M.H., Dexin Wang, and Ziming Li contributed to the detection system setup, secondary beam tuning, experiment operation and data taken. J.H. performed offline data analysis and GEANT4 simulations with the help from Y.Y., J. Lou, X.Y., Q.L., Z.Y., J.X., and Y.G. J.H. and Y.Y. prepared the manuscript, and all co-authors contributed to reviewing the article.

Competing interests

The authors declare no competing interests.

Additional information

Supplementary information The online version contains supplementary material available at https://doi.org/10.1038/s42005-023-01342-6.

Correspondence and requests for materials should be addressed to Yanlin Ye.

Peer review information *Communications Physics* thanks Naoyuki Itagaki and the other, anonymous, reviewer for their contribution to the peer review of this work. A peer review file is available.

Reprints and permission information is available at http://www.nature.com/reprints

Publisher's note Springer Nature remains neutral with regard to jurisdictional claims in published maps and institutional affiliations.